

# Chaos in flexible CubeSat attitude motion due to aerodynamic instability

Vladimir S. Aslanov<sup>a,\*</sup>, Dmitry A. Sizov<sup>a,b</sup>

<sup>a</sup> Samara National Research University, 34, Moscovskoe Shosse, Samara, 443086, Russia

<sup>b</sup> Syzran Branch of Samara State Technical University, 45, Sovetskaya St., Syzran, 446001, Russia

## ARTICLE INFO

### Keywords:

CubeSats  
Deployable panels  
Passive aerodynamic stabilization  
Chaotic attitude dynamics  
LEO

## ABSTRACT

The paper deals with the attitude dynamics of CubeSats with flexible stabilizing panels in free molecular flow taking into account the aerodynamic damping. In addition to the operating position, characterized by zero angle of attack, aerodynamically stabilized satellites may have intermediate equilibrium positions. The presence of unstable equilibrium positions and small perturbations such as the oscillations of the flexible panels is the cause of chaos in the attitude motion. An analysis of the chaotic motion is carried out using Poincaré sections and Lyapunov exponents. Numerical simulations show that the chaos intensity is sensitive to the geometric and environmental parameters of the system.

## 1. Introduction

Initially envisioned as educational or technology demonstration platforms, CubeSats became the basis for real low-cost missions with potential high value in terms of science return and commercial revenue [1,2]. As of April 2021, almost 1500 satellites of this type have been launched [3]. CubeSats come in different sizes, which are based on the standard unit — a cube with side length 10 cm (1U). The most popular are the 3U CubeSats (30 cm × 10 cm × 10 cm), which make up about half of all CubeSats launched [2,3]. CubeSats can be used for several space applications [4], i.e. in astrophysics [5], heliophysics [6], deep space exploration [7,8], communications [9], weather monitoring [10], space debris removal [11,12]. However, one of the most promising and popular applications of CubeSats is Earth observation [13,14] from low and very low Earth orbits (LEO and VLEO). The latter are typically characterized by altitudes of 80–450 km. In the last years, the interest in VLEO has increased because of certain advantages of these orbits: optical payloads can provide higher resolution imagery, the signal to noise ratio for the communications is also higher, VLEO orbits have less population of space debris [15,16].

For most applications, it is important to control angular orientation of LEO and VLEO satellites. Typically, the attitude control is performed using active devices such as magnetorquers and reaction wheels [17], or micropulsed plasma thrusters [18]. However, due to the limited power budgets of CubeSats, the use of such power-consuming devices is challenging. For low orbits, where the influence of the atmosphere is significant, the simplest way is to use the passive aerodynamic

stabilization, since it does not require any power supply. This type of stabilization has been studied since the late 50s [19–25], but previously it was mainly used for large satellites. Currently, with the growing popularity of micro-, nano-, and picosatellites, the number of missions using partial or total aero-stabilization has increased substantially. For example, this type of stabilization is realized for the QARMAN CubeSat [26] currently orbiting the Earth, and the SOAR nanosatellite [27], due to be launched in 2021, meant to investigate the atmospheric flow regime in VLEO. This interest in aerodynamic stabilization stems from the fact that the smaller the satellite, the greater the influence of the aerodynamic torques on its angular motion. It can be shown by the following scaling analysis. The aerodynamic torque is proportional to the cube of the characteristic length, while the moment of inertia of the satellite is proportional to the fifth power of the same quantity. Thus, as the satellite becomes smaller, the moment of inertia decreases faster than the aerodynamic torque, which leads to an increase in angular acceleration due to this torque. Aerodynamic stabilization on CubeSats is usually realized by means of flat tail panels [26,28–33], drag sail systems [12,34], or deployable aeroshells [35]. Hereafter in this paper, only the tail panels will be discussed. All these methods have a common feature: they increase the satellite's drag. For a de-orbit device [32], this can be regarded as an advantage, but in many cases it may be necessary to increase the orbital lifetime. One way to achieve this is to give the satellite a fixed streamlined shape [36], or to use in-orbit deployment of the nose panels forming, e.g., a pyramidal surface [37], as shown in Fig. 1.

Additional deployable aerodynamic surfaces are inevitably flexible

\* Corresponding author.

E-mail addresses: [aslanov\\_vs@mail.ru](mailto:aslanov_vs@mail.ru) (V.S. Aslanov), [sizov.syzran@gmail.com](mailto:sizov.syzran@gmail.com) (D.A. Sizov).

and, while the satellite oscillates under the action of the environmental torques, mainly aerodynamic and gravitational, the panels oscillate as well at frequencies different from that of the satellite. Dynamics of flexible structures and flexible spacecraft problems have received considerable attention in the literature [38–43]. When studying the attitude motion of a spacecraft with flexible appendages, it is convenient to define the unperturbed motion. Typically, it is the attitude motion of the spacecraft with appendages assumed to be rigid. Then the motion of the spacecraft with flexible appendages can be considered as the perturbed motion. It is known that if there are unstable equilibrium positions (saddle points) in the unperturbed motion, then even small disturbances can cause chaos in the perturbed motion [44]. In the case of the attitude motion of a satellite with flexible panels the source of these disturbances is the elastic oscillations of the panels [45–48]. Therefore, in some cases, instead of stabilizing the attitude motion of the satellite, the panels may, on the contrary, destabilize it due to chaos.

New promising trend in the field is the tail panels of variable length [49]. This solution allows to change the moment of inertia of the satellite and, consequently, affect its attitude dynamics. Such new engineering ideas require solving new scientific problems. In particular, the variable length of the panels significantly complicate the aerodynamics of the satellite. The length and deployment angle of the panels, as well as the position of the satellite’s center of mass (CoM), affect the aerodynamic torques and, consequently, the attitude motion. In certain configurations, undesirable intermediate trim positions may exist. The satellite may get to one of these positions because of an accidental disturbance, which may happen, for example, when the satellite separates from the launch vehicle, or if the tail panels are deployed inaccurately. These undesirable intermediate trim positions were discussed earlier [50,51], but the main focus was to ensure the monostability. However, complete elimination of these positions is not always possible, therefore, in the authors’ opinion, more research is needed in the field of attitude motion in the vicinity of these positions, especially considering the possibility of chaos that can be caused by the oscillations of the flexible elements. The other important aspect is the influence of the damping aerodynamic torque. It is often neglected [52,53] since its magnitude is usually much lower than the magnitude of the aerodynamic restoring torque. But in the presence of the intermediate trim positions, especially in VLEO, the damping torque may perturb the attitude motion of the satellite and cause the satellite to get into an undesirable position, characterized by a high angle of attack, and remain in it. So, paradoxically, the damping of attitude motion, which has a positive effect on the angular oscillations near the operating position, may lead to negative consequences if the satellite has intermediate trim positions.

The goal of the paper is to investigate the features of the nonlinear attitude motion of flexible CubeSats under aerodynamic torques at large angles of attack in the vicinity of the intermediate equilibrium positions and to demonstrate the possibility of chaos. In order to achieve this goal, the unperturbed and perturbed motions are defined, the equilibrium positions are studied, the aerodynamic characteristics of CubeSats with nose and tail panels are calculated, the mathematical model of the nonlinear attitude motion of the system is developed, and numerical

simulations are performed.

The paper is organized as follows. In Section 2 the problem is formulated and the unperturbed motion is analyzed. The dependencies of equilibrium positions on the orbit altitude and the length of the tail panels are studied. Section 3 presents the equations of perturbed motion of the satellite with flexible panels, which take into account the action of restoring and damping aerodynamic torques as well as the gravitational torque. Section 4 contains numerical simulations. Chaos is investigated using Poincaré sections and Lyapunov exponents. Finally, conclusions are given in Section 5.

## 2. Problem statement. Aerodynamic instability

Consider the attitude motion of a CubeSat with additional aerodynamic surfaces under the following assumptions.

1. The attitude motion of the satellite depends on two environmental torques: one due to the gravity gradient and one due to the influence of atmosphere.
2. The satellite has two equal principal moments of inertia ( $J_y = J_z$ ,  $J_z > J_x$ ).
3. The center of mass of the satellite lies on its longitudinal axis.
4. Additional aerodynamic surfaces are modeled as homogeneous thin flat plates.
5. The aerodynamic characteristics of the satellite do not depend on the oscillations of the panels.
6. The orbit of the satellite remains circular.
7. All motions take place in the orbital plane.

The last assumption is reasonable because to demonstrate chaos in the attitude motion, it is enough to take the simplest case of rotation in the orbital plane, since the presence of chaos in a particular case means that it is actually present in the general case. In addition, the planar rotation is the limiting case of the spatial attitude motion. It is in the planar case that the largest amplitudes of the angle of attack are observed, since all the potential energy of attitude motion stored in the satellite is transformed into the kinetic energy of rotation around only one axis.

Let us determine the environmental torques acting on the satellite. The gravity gradient torque is defined as

$$M_g(h, \theta) = 3(J_z - J_x)\nu^2 \cos\theta \sin\theta \tag{1}$$

where  $\theta$  is the angle of attack,  $J_z$  and  $J_x$  are transverse and longitudinal moments of inertia of the satellite, respectively,  $\nu = \sqrt{\mu/(R+h)^3}$  is the mean motion,  $h$  is the altitude,  $R$  and  $\mu$  are the mean radius and gravitational parameter of the Earth, respectively. Note that the gravitational torque is conservative (potential), since it depends only on the coordinates  $\theta$  and  $h$ .

The aerodynamic torque  $M_a$  can be written as a sum of two components:

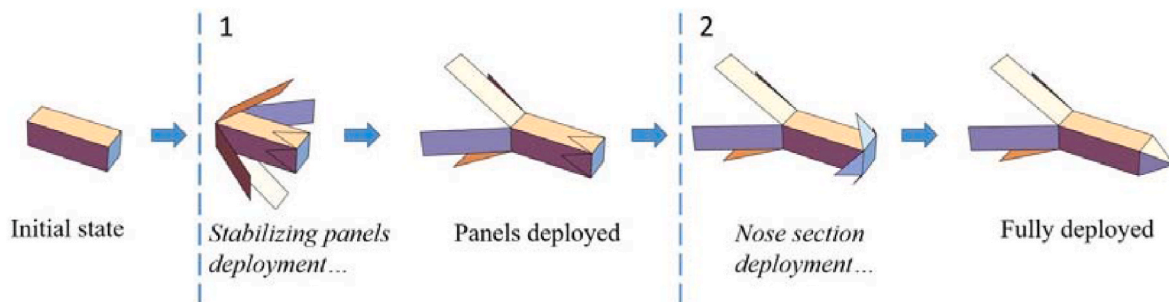


Fig. 1. Concept of CubeSat with deployable tail and nose panels [37].

$$M_a(h, \theta, \dot{\theta}) = M_r(h, \theta) + M_d(h, \theta, \dot{\theta}) \tag{2}$$

where  $M_r$  is the restoring torque, which is conservative,

$$M_r(h, \theta) = C_m(\theta) \frac{\rho V(h)^2}{2} l A, \tag{3}$$

and  $M_d$  is the damping torque, which is non-conservative since it depends not only on the coordinates, but also on the angular speed:

$$M_d(h, \theta, \dot{\theta}) = C_m^{\dot{\theta}}(\theta) \frac{\rho V(h)^2 l^2 A \dot{\theta}}{2} \tag{4}$$

In Eqs. (3) and (4)  $A$  is the reference area taken equal to the satellite body cross-section area,  $l$  is the reference length taken equal to the satellite body length,  $\rho$  is the air density,  $V = \sqrt{\mu/(R+h)}$  is the orbital velocity,  $C_m$  and  $C_m^{\dot{\theta}}$  are the restoring and damping aerodynamic torque coefficients, respectively.

The aerodynamic torque coefficients are calculated as follows. Taking into account that at the CubeSats operational altitudes (above 120 km) the Knudsen number  $Kn$  is larger than 10, which means that the flow is free molecular [54], one can assume that the reflected air molecules speed distribution is Maxwellian and calculate the pressure and shear stress coefficients using the Schaaf and Chambre's approach [55]. Dividing the surface of the satellite into a number of small flat elements we find pressure and shear stress coefficients for each element,  $c_{p_i}$  and  $c_{\tau_i}$ , respectively, as

$$c_{p_i} = \left[ \frac{2 - \sigma_N}{s\sqrt{\pi}} \sin \theta_i + \frac{\sigma_N}{2s^2} \sqrt{\frac{T_w}{T_\infty}} \right] \exp(-s^2 \sin^2 \theta_i) + \left[ \frac{(2 - \sigma_N)}{s^2} \left( \frac{1}{2} + s^2 \sin^2 \theta_i \right) + \frac{\sigma_N}{2s} \sqrt{\frac{T_w}{T_\infty}} \sqrt{\pi} \sin \theta_i \right] [1 + \operatorname{erf}(s \sin \theta_i)], \tag{5}$$

$$c_{\tau_i} = \frac{\sigma_T \cos \theta_i}{s\sqrt{\pi}} (\exp(-s^2 \sin^2 \theta_i) + [1 + \operatorname{erf}(s \sin \theta_i)] s \sqrt{\pi} \sin \theta_i) \tag{6}$$

where  $i$  is the element number,  $s$  is the freestream molecular speed ratio,

$$s = \frac{V}{\sqrt{2RT_\infty}}, \tag{7}$$

$R = 287 \text{ J/(kg}\cdot\text{K)}$  is the ideal gas constant for air,  $T_w$  is the wall temperature,  $T_\infty$  is the temperature of incident stream,  $\sigma_N$  and  $\sigma_T$  are the normal and tangential momentum accommodation coefficients, respectively. For interaction of air with most engineering surfaces, experimental data indicate that  $\sigma_N \approx \sigma_T \approx 1$  [56]. In this paper, these coefficients are taken both equal to 0.9 which corresponds to aluminum-air interaction [57]. In Eqs. (5) and (6),  $\theta_i$  is the inclination angle of the  $i$ -th flat element,

$$\theta_i = \arccos(\hat{\tau}_i \cdot \hat{\mathbf{V}}) \tag{8}$$

where  $\hat{\mathbf{V}}$  is the unit vector of the incident stream,  $\hat{\tau}_i$  is the unit tangential vector of the  $i$ -th element,

$$\hat{\tau}_i = \frac{\hat{\mathbf{V}} - (\hat{\mathbf{n}}_i \cdot \hat{\mathbf{V}}) \hat{\mathbf{n}}_i}{\|\hat{\mathbf{V}} - (\hat{\mathbf{n}}_i \cdot \hat{\mathbf{V}}) \hat{\mathbf{n}}_i\|}, \tag{9}$$

$\hat{\mathbf{n}}_i$  is the unit normal vector of the  $i$ -th element directed such a way that  $\hat{\mathbf{n}}_i \cdot \hat{\mathbf{V}} \geq 0$ . Restoring torque coefficient is calculated as

$$C_m = \frac{1}{Al} \sum_{i=1}^N A_i \left[ \mathbf{r}_i \times (c_{p_i} \hat{\mathbf{n}}_i + c_{\tau_i} \hat{\tau}_i) \right] \cdot \hat{\mathbf{z}} \tag{10}$$

where  $\mathbf{r}_i$  is the radius-vector from the satellite center of mass to the geometric center of the  $i$ -th element,  $\hat{\mathbf{z}}$  is the unit vector along the

satellite transverse axis  $z$ ,  $N$  is the number of elements. Note that it is necessary to exclude from consideration the elements that are shielded by the upstream components of the body. An example of surface meshing with shielding taken into account is shown in Fig. 2. Taking into account that, as the satellite rotates with angular velocity  $\omega$ , the speed of the incident stream on the  $i$ -th element changes by a small amount ( $\omega \times \mathbf{r}_i$ ), one can calculate the damping torque coefficients (see, e.g., Ref. [58]).

In the case of planar rotation, we have only one damping torque coefficient corresponding to the rotation about  $z$  axis with angular speed  $\dot{\theta}$ :

$$C_m^{\dot{\theta}} = \frac{\partial C_m}{\partial \bar{\omega}_z} \tag{11}$$

where  $\bar{\omega}_z$  is the dimensionless angular speed,

$$\bar{\omega}_z = \frac{l}{V} \dot{\theta}. \tag{12}$$

For the convenience of analysis, the aerodynamic torque coefficients can be represented by Fourier series:

$$C_m(\theta) = \sum_{j=1}^k b_{\theta_j} \sin j\theta, \tag{13}$$

$$C_m^{\dot{\theta}}(\theta) = \frac{a_{\dot{\theta}_0}}{2} + \sum_{j=1}^k a_{\dot{\theta}_j} \cos j\theta \tag{14}$$

where  $k$  is the number of harmonics.

We define the perturbed attitude motion as the motion of the satellite with flexible panels under the restoring and damping aerodynamic torques and gravitational torque. Then the unperturbed motion is the motion of the rigid body under the aerodynamic restoring torque and gravitational torque only. Taking into account Eqs. (1), (3) and (13) one can write the equation of the unperturbed motion as

$$J_z \ddot{\theta} = M_r + M_g = c_a \sum_{j=1}^k \sin j\theta + c_g \sin 2\theta \tag{15}$$

where

$$c_a = \frac{1}{2} \rho V^2 l A, \tag{16}$$

$$c_g = \frac{3}{2} (J_z - J_x) \nu^2. \tag{17}$$

Note that all the torques acting in the unperturbed motion are potential, so Eq. (15) has an energy integral, which can be written as

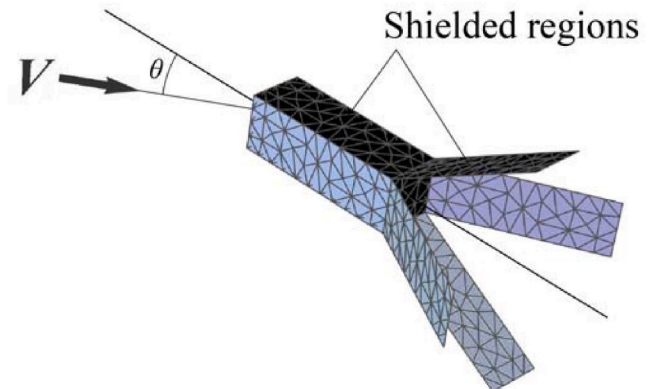


Fig. 2. Example of satellite surface meshing and shielding.

$$E = \frac{1}{2} J_c \dot{\theta}^2 + U_s(\theta) = const \tag{18}$$

where  $U_s$  is the potential energy of the satellite in its unperturbed motion,

$$U_s(\theta) = - \int (M_r + M_g) d\theta = c_a \sum_{j=1}^k \frac{b_{\theta j}}{j} \cos^j \theta + c_g \cos^2 \theta. \tag{19}$$

Minima and maxima of the  $2\pi$ -periodic potential energy function defined by Eq. (19) correspond to the equilibrium positions  $\theta_e$  of the satellite which are the roots of the equation  $M_r + M_g = -\frac{\partial U_s}{\partial \theta} = 0$ . When

$$\left. \frac{\partial^2 U_s}{\partial \theta^2} \right|_{\theta=\theta_e} > 0, \text{ the potential energy is in its minimum and the equilibrium}$$

is stable; on the contrary, when  $\left. \frac{\partial^2 U_s}{\partial \theta^2} \right|_{\theta=\theta_e} < 0$ , the potential energy is at its maximum so the equilibrium is unstable.

Potential energy curves may have different shapes depending on the altitude and satellite parameters, primarily on the coefficients  $b_{\theta j}$  of the Fourier series representation of the restoring aerodynamic torque coefficient. These coefficients, in their turn, are determined by the geometric parameters of the satellite, so it is difficult to analyze the unperturbed motion without choosing a particular shape of the satellite. In this paper, we consider a CubeSat with pyramidal nose and tail panels (Fig. 3). The most important of its geometric parameters are the satellite body length  $l$ , panels deployment angle  $\delta$ , the dimensionless nose and tail panels lengths  $\lambda_n$  and  $\lambda_t$ , respectively, dimensionless longitudinal shifts of the CoM of the satellite body and of the CoM of the entire satellite from the geometric center  $C_1$ ,  $\Delta_b$  and  $\Delta$ , respectively. Parameters  $\Delta$  and  $\Delta_b$  are considered positive if the centers of mass are shifted closer to the nose of the satellite. The longitudinal shift of the CoM of the satellite can be calculated using the definition of CoM as

$$\Delta = \frac{\Delta_b + 2 \left( 1 + \frac{2}{3} \lambda_n \right) \mu_n - 2 \mu_t (1 + \lambda_t \cos \delta)}{1 + 4(\mu_n + \mu_t)} \tag{20}$$

where  $\mu_t$  is the relative mass of a single tail panel,

$$\mu_t = \frac{m_t}{M} = \frac{\sigma_t \lambda_t l^2}{M u}, \tag{21}$$

$\mu_n$  is the relative mass of a single nose panel,

$$\mu_n = \frac{m_n}{M} = \frac{\sigma_n \lambda_n l^2}{2 M u \cos \alpha}, \tag{22}$$

$\alpha$  is the angle between the nose panel and the longitudinal axis of the satellite,

$$\alpha = \arctan \left( \frac{a}{2 \lambda_n l} \right) = \arctan \left( \frac{1}{2 \lambda_n u} \right), \tag{23}$$

$m_t$  is the mass of the tail panel,  $m_n$  is the mass of the nose panel,  $\sigma_t$  is the tail panel mass per unit area,  $\sigma_n$  is the nose panel mass per unit area,  $M$  is the mass of the satellite body,  $u$  is the number of standard 1U units in the satellite, which are supposed to be arranged in a single row,  $a = l/u$  is the standard unit side length.

Let us analyze typical equilibrium positions and potential energy curves for the unperturbed motion on the example of three 3U CubeSats with pyramidal nose and tail panels of different lengths (Fig. 4). Their parameters are given in Table 1. Fig. 5 represents the dependencies of the positions of stable and unstable equilibria,  $\theta_s$  and  $\theta_u$ , respectively, on the orbit altitude for the three CubeSats considered. Below a certain critical altitude, which for the discussed satellites is about 600 km, the aerodynamic torque prevails. As it tends to align the satellite along the orbital velocity vector, the position  $\theta = \theta_0 = 0$  is stable. After passing the critical altitude, the aerodynamic stabilization is no longer effective, and the gravity gradient torque, which tends to align the satellite along the local vertical, becomes more significant. For this reason, the satellites with relative panel lengths of 5/6 and 1 have two stable positions in the vicinity of  $-\pi/2$  and  $\pi/2$ . Similar case has been considered in Ref. [48]. Note that in the case of short panels ( $\lambda_t = 2/3$ ) the intermediate stable equilibrium positions  $\theta_s$  are determined primarily by the aerodynamics of the satellite and exist even in low orbits (blue solid curves in Fig. 5). Unlike the satellites with long panels, the satellites with short panels have not only stable, but also unstable equilibrium positions  $\theta_u$  (blue dashed curves in Fig. 5). In order to better illustrate the nature of these intermediate equilibrium positions, let us examine the torques acting on the satellite in the unperturbed motion and the corresponding potential energy  $U_s$  (Fig. 6). Since both the aerodynamic and gravitational torques depend on the orbit altitude, in order to better illustrate the nature of these intermediate equilibrium positions, one needs to choose a particular altitude below the critical one. Hereinafter, we take the altitude equal to 250 km. Fig. 6, top represents the sum of aerodynamic restoring torque about the CoM of the satellite  $M_r$ , and gravitational torque  $M_g$ . Environmental parameters necessary to calculate the aerodynamic moment are taken from Table 2 for the case of high solar activity. It can be seen that the greater the length of the panels, the greater the magnitude of the sum of torques. At the same time, the tail panels length does not change the character of the given dependencies. The kinks in the graphs correspond to the angular positions where the shielding of some elements of the satellite begins or ends. Note that the shape of the restoring torque curves is consistent with the data of other researchers [35,50,51]. Fig. 6, top shows that in the case of short panels the sum of torques is positive when  $\theta = \pi/2$  and negative when  $\theta = -\pi/2$  (blue curve in Fig. 6, top), and consequently, there are intermediate equilibrium positions. Fig. 6, bottom shows that for all considered panel

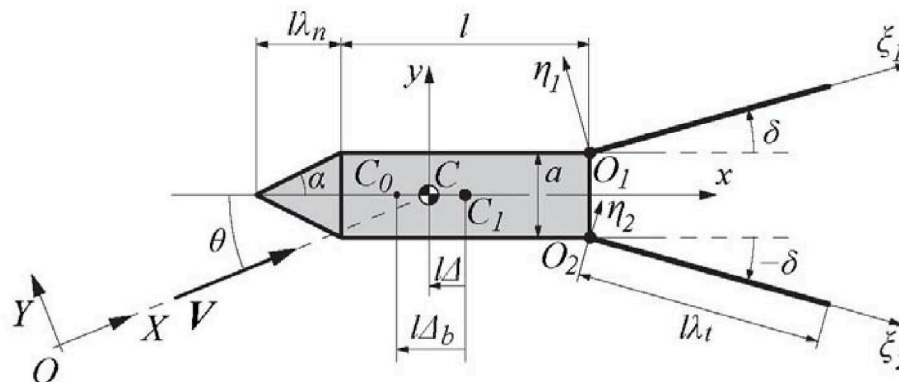


Fig. 3. CubeSat with deployable side panels. For clarity, only two panels are depicted.

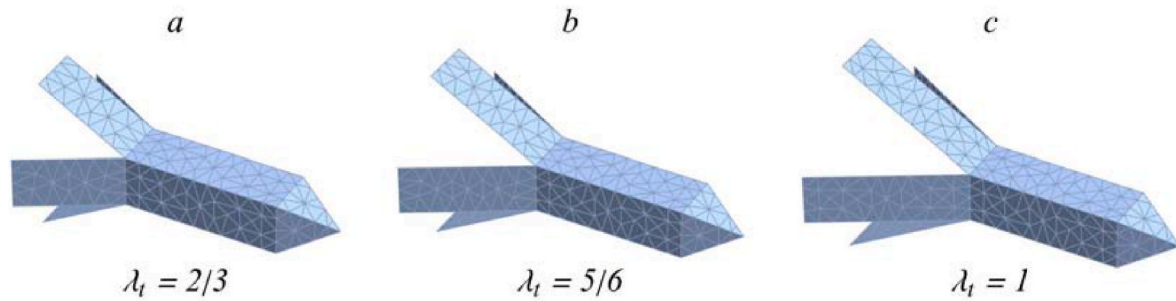


Fig. 4. 3U CubeSats with nose and tail panels.

Table 1

CubeSat parameters.

Parameter	Value
Number of standard units $u$	3
Satellite body length $l$	0.3 m
Satellite body width $a$	0.1 m
Reference area $A$	0.01 m <sup>2</sup>
Satellite body mass $M$	4 kg
Longitudinal moment of inertia of satellite body $J_{x0}$	0.0067 kg m <sup>2</sup>
Transverse moment of inertia of satellite body $J_{z0}$	0.0333 kg m <sup>2</sup>
Relative longitudinal shift of satellite body CoM $\Delta_b$	-0.25
Nose relative length $\lambda_n$	1/3
Tail panels relative length $\lambda_t$	2/3; 5/6; 1
Tail panels deployment angle $\delta$	30°
Nose and tail panels material	Aluminum
Nose and tail panels density	2700 kg/m <sup>3</sup>

lengths, the stable operational position  $\theta_0$  corresponds to a potential well, as it can be expected. At the same time, in the case of short panels, there exist additional local potential wells corresponding to the intermediate stable equilibrium positions. This case is of particular interest, so we will refer to the CubeSat with  $\lambda_t = 2/3$  shown in Fig. 4, a as the example CubeSat. Its other parameters are given in Table 1. In Fig. 7, the above-mentioned potential energy curve for the example CubeSat is shown along with the phase portrait of the unperturbed system, which has two separatrices. The outer separatrix correspond to the unstable equilibrium positions  $\theta = \pm \pi$  and the total energy  $E = U_{max}$ . The inner separatrix correspond to the unstable equilibrium positions  $\theta = \pm \theta_u$  and the total energy  $E = U_u$ . The determination of these unperturbed separatrices is important for further study of chaos in the perturbed

motion. This is due to the fact that, although the thickness of the chaotic layer depends in a complex way on the system parameters, near the separatrices, chaos will occur even if the chaotic layer width is small.

In order to investigate the perturbed motion in the vicinity of the separatrices, one needs to derive the equations of motion of the system taking into account flexibility of the tail panels and the damping aerodynamic torque, which is the goal of the next section.

### 3. Equations of motion

In this paper, we use four coordinate frames (Fig. 3): the orbital frame  $OXY$ , the satellite body-fixed frame  $Cxy$  and two panel-fixed frames  $O_1\xi_1\eta_1$  and  $O_2\xi_2\eta_2$ . The angles  $\delta$  between the axes  $Cx$  and  $O_1\xi_1$  and  $-\delta$  between the axes  $Cx$  and  $O_2\xi_2$  can also be regarded as the panel deployment angles. The coordinates of the pivot points of the panels  $O_1$  and  $O_2$  in the  $Cxy$  frame are  $(l_c, a/2)$  and  $(l_c, -a/2)$ , respectively, where,  $l_c = (\Delta + 1/2)l$ .

The kinetic energy of the nanosatellite is composed of the kinetic energy of the satellite body  $T_b$  and the kinetic energy of the flexible side panels  $T_p$ , which are modeled as cantilever beams:

$$T = T_b + T_p. \tag{24}$$

The kinetic energy of the attitude motion of the nanosatellite is defined as

$$T_b = \frac{1}{2} J_z \dot{\theta}^2. \tag{25}$$

The kinetic energy of the flexible side panels is

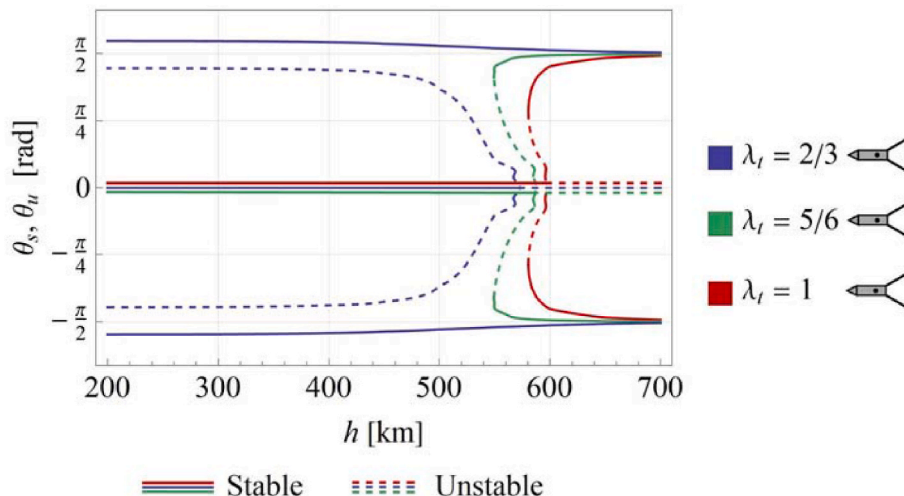


Fig. 5. Equilibrium positions of 3U CubeSats with nose and tail panels. For visualization purposes, the overlapping lines corresponding to  $\theta = 0$  are shown separated.

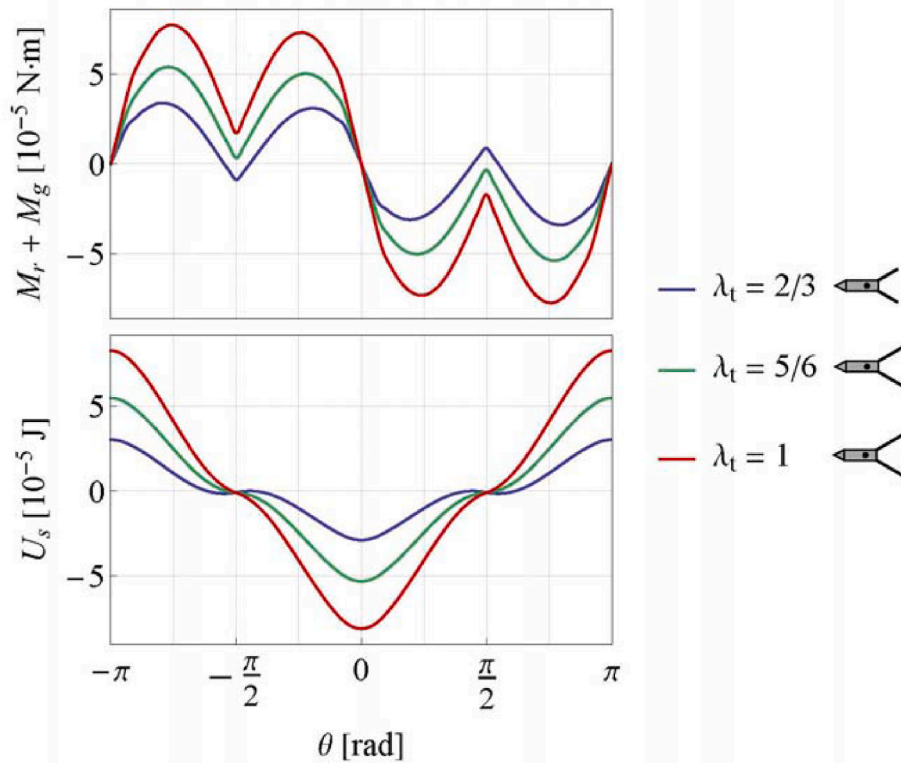


Fig. 6. Sum of gravitational and restoring aerodynamic torque and potential energy for 3U CubeSats with nose and tail panels ( $h = 250$  km).

Table 2

Environmental parameters corresponding to an altitude of 250 km.

Parameter	Value		
	Low solar activity (SA)	Mean SA	High SA
Air density $\rho [10^{-11} \text{ kg/m}^3]$	2.1	7.8	16
Incident stream temperature $T_\infty$ [K]	690	890	1240
Wall temperature $T_w$ [K]	300		

$$T_p = \frac{1}{2} \int_0^{l_p} (\mathbf{V}_{p1}^2 + \mathbf{V}_{p2}^2) dm \quad (26)$$

where  $l_p = \lambda_t$  is the length of the panel,  $\mathbf{V}_{pi}$  is the velocity of a differential mass element of the flexible panel relative to the center of mass,  $i = 1, 2$ . According to Fig. 3,  $\mathbf{V}_{pi}$  can be written as

$$\mathbf{V}_{p1} = \frac{d}{dt} \left[ \begin{pmatrix} c\theta & -s\theta \\ s\theta & c\theta \end{pmatrix} \cdot \left( \begin{bmatrix} l_c \\ a \end{bmatrix} \frac{1}{2} + \begin{pmatrix} c\delta & -s\delta \\ s\delta & c\delta \end{pmatrix} \cdot [\xi_1, \eta_1]^T \right) \right] \quad (27)$$

$$\mathbf{V}_{p2} = \frac{d}{dt} \left[ \begin{pmatrix} c\theta & -s\theta \\ s\theta & c\theta \end{pmatrix} \cdot \left( \begin{bmatrix} l_c \\ -a \end{bmatrix} \frac{1}{2} + \begin{pmatrix} c\delta & s\delta \\ -s\delta & c\delta \end{pmatrix} \cdot [\xi_2, \eta_2]^T \right) \right] \quad (28)$$

where  $\xi_i, \eta_i$  are the longitudinal and transverse coordinates of the differential mass element  $dm$  of the flexible panel, respectively. The deflection of the flexible panel is defined as

$$\eta_i(\xi_i, t) = \sum_{j=1}^N \Phi_j(\xi_i) q_{ij}(t), \quad i = 1, 2 \quad (29)$$

where  $q_{ij}(t)$  are modal coordinates,  $N$  is the number of modes considered, and  $\Phi_j(\xi_i)$  are the shape functions. The following shape function is

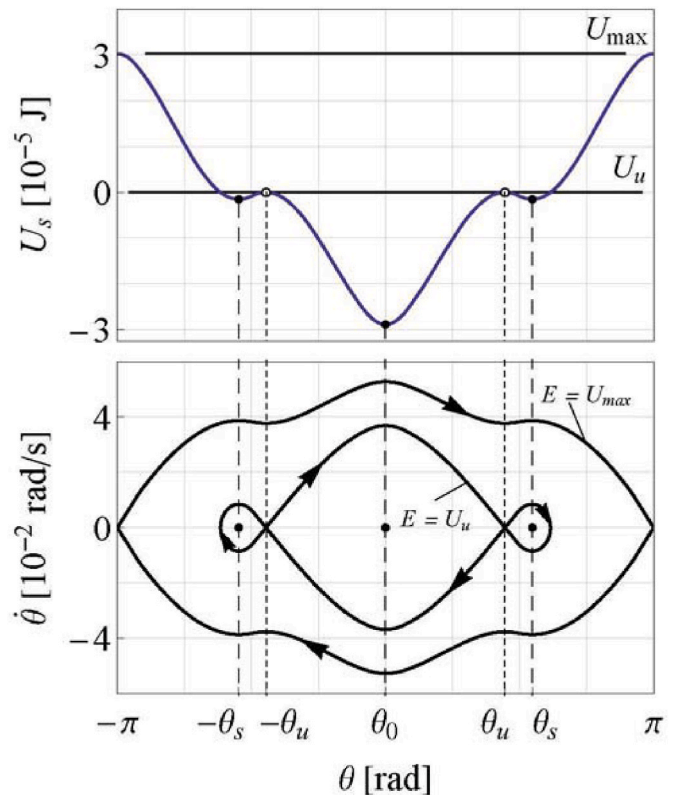


Fig. 7. Potential energy, equilibrium positions, and phase portrait of the example CubeSat ( $h = 250$  km).

an acceptable candidate for a clamped beam [59]:

$$\Phi_j(\xi_i) = B_j \left[ \cosh \frac{\omega_j^{1/2} \xi_i}{l_p} - \cos \frac{\omega_j^{1/2} \xi_i}{l_p} - d_j \left( \sinh \frac{\omega_j^{1/2} \xi_i}{l_p} - \sin \frac{\omega_j^{1/2} \xi_i}{l_p} \right) \right] \quad (30)$$

where  $B_j$  is an unessential constant multiplier taken so that  $\Phi_j(l_p) = 1$ ,

$$d_j = \frac{\cos \omega_j^{1/2} + \cosh \omega_j^{1/2}}{\sin \omega_j^{1/2} + \sinh \omega_j^{1/2}}, \quad (31)$$

$\omega_j$  is a nondimensional natural frequency. For a clamped beam,  $\omega_j$  is defined by the equation [59].

$$\cos \omega_j^{1/2} \cosh \omega_j^{1/2} = -1 \quad (32)$$

where  $\omega_1 = 3.51$ ,  $\omega_2 = 22.03$ ,  $\omega_3 = 61.70$ , ... are the roots of equation (32).

The potential energy of the satellite equals the sum of the potential energy of the satellite body and the flexible panels, and it can be written as

$$U(h, \theta, \eta_i) = U_s(h, \theta) + U_p(\eta_i), \quad (33)$$

where

$$U_p(\eta_i) = \int_0^{l_p} \left[ \sum_{i=1}^2 EJ \left( \frac{\partial^2 \eta_i}{\partial \xi_i^2} \right)^2 \right] d\xi_i, \quad (34)$$

$EJ$  is the bending stiffness of the flexible panels,  $E$  is the Young's modulus,  $J$  is the area moment of inertia of panel cross-section,

$$J = \frac{ab^3}{12}, \quad (35)$$

$b$  is the panel thickness, and the functions  $U_s$  and  $\eta_i$  are defined by equations (19) and (29), respectively.

We use the Lagrangian formalism to write the motion equations of the system

$$\frac{d}{dt} \frac{\partial L}{\partial \dot{s}_n} - \frac{\partial L}{\partial s_n} = Q_n, \quad n = 1, \dots, 1 + 2N \quad (36)$$

where  $L = T - U$  is the Lagrange function,  $s = (\theta, q_{11}, q_{21}, \dots, q_{1N}, q_{2N})$  is the vector of generalized coordinates,  $Q$  is the vector of non-potential generalized forces. Let us consider only the case when  $N = 1$ , and taking into account Eqs. (16), (17), (19) and (24)–(34) write the Lagrange function in the following simple form:

$$L = \frac{1}{2} a_\theta \dot{\theta}^2 + a_{\theta q} (\dot{q}_1 + \dot{q}_2) \dot{\theta} + \frac{1}{2} a_q (\dot{q}_1^2 + \dot{q}_2^2) - c_a \sum_{j=1}^k \frac{b_j}{j} \cos j\theta - c_\delta \cos^2 \theta - \frac{1}{2} c_q (q_1^2 + q_2^2) \quad (37)$$

where

$$a_\theta = J_{z1} + 2\mu_{tl} l_p \left[ \frac{1}{3} l_p^2 + l_p \left( \frac{a}{2} \sin \delta + l_c \cos \delta \right) + \left( \frac{a}{2} \right)^2 + l_c^2 \right], \quad (38)$$

$$a_{\theta q} = l \mu_{tl} \left[ I_1 \left( \frac{a}{2} \sin \delta + l_c \cos \delta \right) + I_3 \right], \quad (39)$$

$$a_q = l^2 \mu_{tl} I_2, \quad (40)$$

$$c_q = EJ l_p^2 I_4, \quad (41)$$

$J_{z1}$  is the total moment of inertia of the rigid parts of the satellite,  $\mu_{tl}$  is the linear mass of a single tail panel,

$$\mu_{tl} = \frac{\sigma_t l}{u l_t}, \quad (42)$$

$q_1 = q_{11}/l_p, q_2 = q_{21}/l_p$  are the dimensionless modal coordinates,

$$I_1 = \int_0^{l_p} \Phi_1(\xi) d\xi, \quad (43)$$

$$I_2 = \int_0^{l_p} \Phi_1^2(\xi) d\xi, \quad (44)$$

$$I_3 = \int_0^{l_p} \xi \Phi_1(\xi) d\xi, \quad (45)$$

$$I_4 = \int_0^{l_p} \Phi_1''(\xi)^2 d\xi, \quad (46)$$

$$\Phi_1(\xi) = B \left[ \cosh \frac{\omega^{1/2} \xi}{l_p} - \cos \frac{\omega^{1/2} \xi}{l_p} - d \left( \sinh \frac{\omega^{1/2} \xi}{l_p} - \sin \frac{\omega^{1/2} \xi}{l_p} \right) \right], \quad (47)$$

$\omega = 3.51, d = 0.734, B = 0.5006$ . The non-potential generalized forces are

$$Q = (M_d, 0, 0) \quad (48)$$

where the damping aerodynamic torque  $M_d$  is defined by Eq. (4).

#### 4. Numerical simulations

In this section, the chaotic motion of a flexible CubeSat will be studied using Poincaré sections and Lyapunov exponents. Along with these tools, the Melnikov criterion is often used to determine the presence of chaos in a system. Melnikov's theory allows to write the necessary condition for chaos [60,61]. However, the construction of the Melnikov criterion is difficult for the considered unperturbed system due to the lack of analytical expressions for its heteroclinic trajectories.

All numerical simulations of the perturbed nonlinear attitude motion of the example CubeSat (Fig. 4,a) will be performed for a circular orbit with an altitude of 250 km, unless otherwise specified. The density and temperature of the incident stream at this altitude are chosen using Jacchia-Bowman 2008 Atmosphere Model [62] for different levels of solar activity. The temperature of the satellite's surfaces is taken equal to  $T_w = 300$  K based on the energy balance between an aluminum satellite surface and the solar flux [63], which is consistent with actual in-orbit measurements for CubeSats [64]. For convenience, all environmental data used are gathered in Table 2. Fig. 8 shows typical dependencies of the restoring and damping aerodynamic torque coefficients on the angle of attack for the example satellite, calculated numerically using Eqs. (10) and (11), respectively, as well as the data from Table 2. Other parameters of the example CubeSat are given in Table 1.

Fig. 9 depicts three trajectories on a phase plane  $(\theta, \dot{\theta})$  starting at the same point  $(0, 0.0367)$  near the inner separatrix (see Fig. 7, bottom) and calculated for three different sets of initial conditions of the panels oscillations:

$$q_{10} = 0.007, q_{20} = 0.022; q_{10} = -0.002, q_{20} = -0.005; q_{10} = -0.019, q_{20} = -0.039.$$

For all three cases, we take  $\dot{q}_{10} = \dot{q}_{20} = 0$ . Each phase trajectory demonstrates that the damping torque dissipates the energy of the system and pulls the satellite into one of the potential wells. Even though the phase trajectories start at the same point, the satellite eventually oscillates about different stable equilibrium positions. In the first case, it is an intermediate trim position  $\theta = \theta_s$ , in the second case, it is the operational position  $\theta = \theta_0$ , and in the third case, it is another intermediate trim position  $\theta = -\theta_s$ . This qualitative difference between the

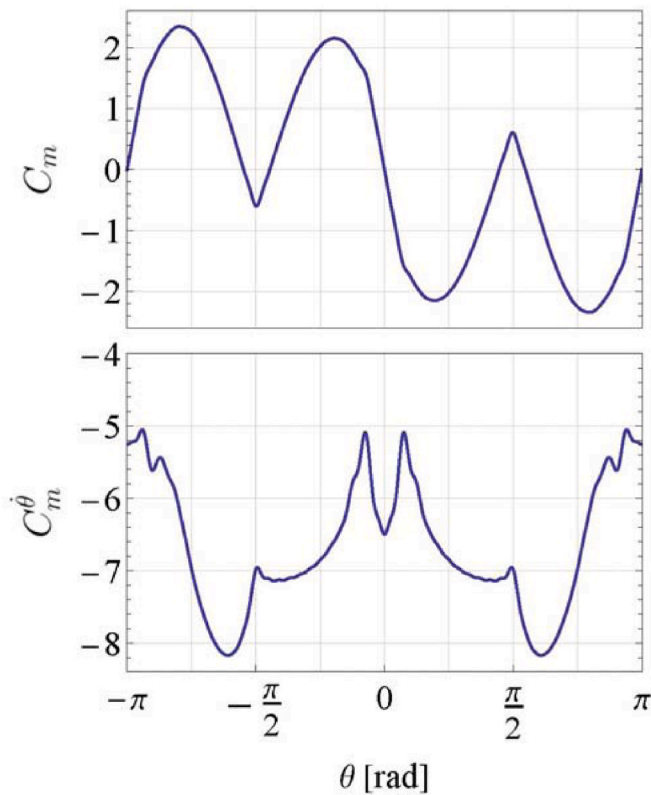


Fig. 8. Coefficients of restoring (top) and damping (bottom) aerodynamic torques for the example CubeSat ( $h = 250$  km, high solar activity).

trajectories is clearly due to the difference in the initial disturbances of the panels. Thus, Fig. 9 demonstrates that the perturbed system is sensitive to initial conditions, which is one of the attributes of chaos. Fig. 9 also shows that the oscillations of the satellite body have a high-frequency harmonic of small amplitude caused by the flexible panels. Fig. 10 illustrates the oscillations of the panels themselves, and it can be clearly seen that they oscillate in antiphase. For convenience, we plot here the panels' tips maximum deflections instead of non-dimensional coordinates  $q_1$  and  $q_2$ .

Perturbations in the satellite angular motion due to the panels oscillations lead to a complication of the phase space and occurrence of a chaotic layer near the unperturbed separatrices. The intersection of stable and unstable manifolds can be revealed in the Poincaré plane [61]. Fig. 11 depicts Poincaré sections for the perturbed motion. Note that the phase trajectories simulated to plot the cloud of points start from the points lying in one of the intermediate potential wells near the separatrix. The fact that some of cross-section points appear in the

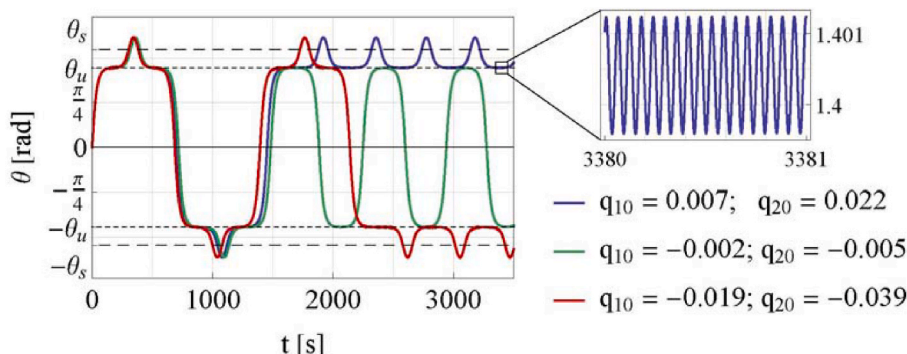


Fig. 9. Phase trajectories for the example CubeSat.

central area between the saddle points  $-\theta_u$  and  $\theta_u$  indicates that the phase trajectories cross the separatrix and pass from one potential well to another. Therefore, the occurrence of chaos in the perturbed system is verified.

In addition to constructing Poincaré sections, the presence of chaos in the system can be confirmed by calculating the Lyapunov spectrum for individual trajectories. The Lyapunov exponents making up this spectrum characterize the evolution of trajectories in a certain volume near the trajectory under consideration in different directions of the phase volume. A numerical algorithm for calculating Lyapunov exponents is given, for example, in Ref. [65]. Chaotic motion must produce at least one positive Lyapunov exponent, hence it is sufficient to calculate only the maximum Lyapunov exponent. Fig. 12 shows maximum Lyapunov exponents for the phase trajectories starting at a saddle point  $(\theta_u, 0)$  without initial panels disturbances for three different orbit altitudes assuming mean solar activity. All the exponents are positive, which indicates chaos. Note that at the altitudes 200 and 300 km the magnitude of the Lyapunov exponent is lower, so the chaotic effects are weaker than at 250 km. At lower altitudes, this is due to the increasing role of the damping aerodynamic torque. At higher altitudes, this is caused by an increase in the ratio between the frequencies of oscillations of the panels and the satellite body and, accordingly, by a decrease in the influence of the elastic oscillations of the panels on the attitude motion of the satellite.

Fig. 12 thus confirms that the previously chosen altitude of 250 km allows a better illustration of the chaos in attitude motion of the example satellite. Figs. 13 and 14 show maximum Lyapunov exponents for the phase trajectories starting at the same saddle points. Fig. 13 depicts the exponents calculated for three different levels of solar activity, and consequently, air density (see Table 2). It can be seen that, at a given altitude, the system is somewhat more prone to chaotic behavior when the incident stream density is low. This is due to the fact that, in this case, since the aerodynamic forces are weaker, the effect of the perturbations caused by the oscillations of the panels increases. The exponents

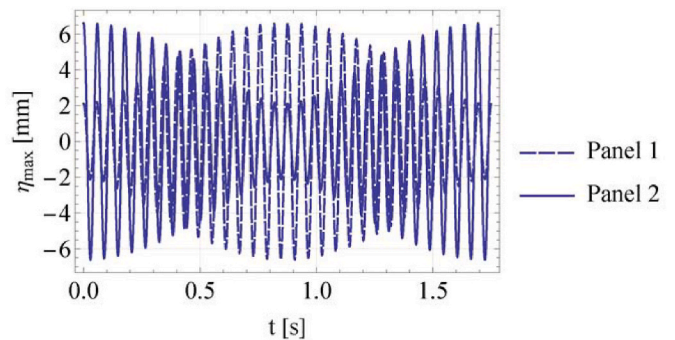
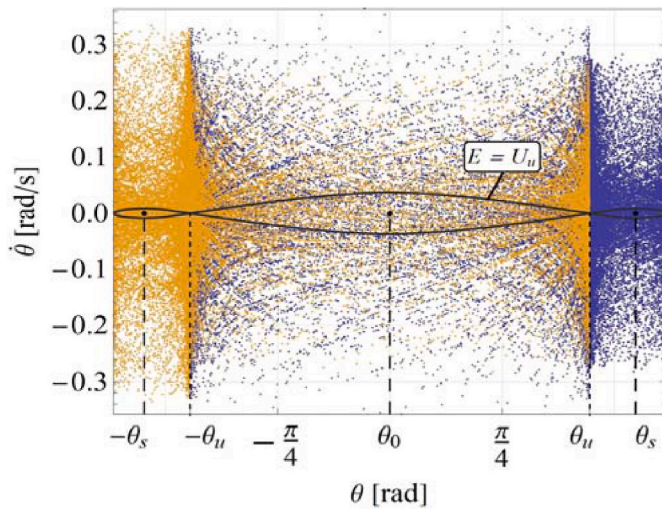
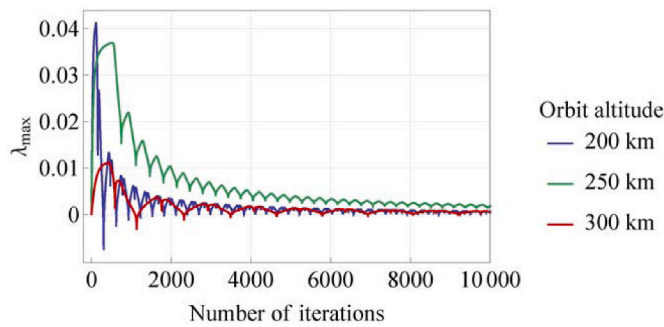


Fig. 10. Typical time histories of panel tips deflection for the example CubeSat.





**Fig. 11.** Poincaré sections for the example CubeSat: blue – start from right potential well, orange – start from left potential well. Solid black line represents the inner unperturbed separatrix (see also Fig. 7). (For interpretation of the references to colour in this figure legend, the reader is referred to the Web version of this article.)



**Fig. 12.** Maximum Lyapunov exponents for the example CubeSat at three different altitudes.

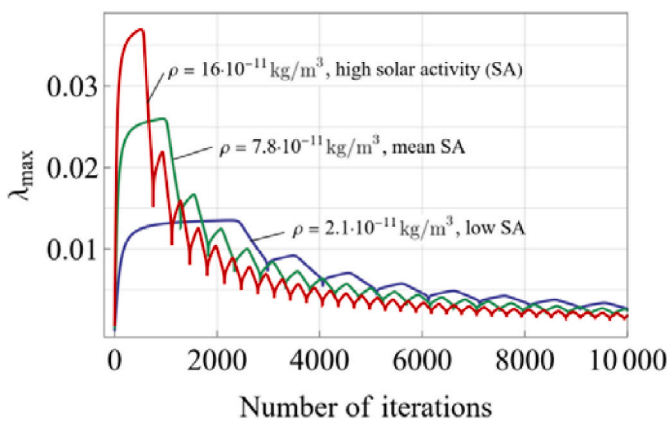


**Fig. 13.** Maximum Lyapunov exponents for the example CubeSat at three different levels of solar activity.

shown in Fig. 14 are calculated for four different values of tail panels thickness. As in the previous case, all the exponents are positive, so the behavior of the system is chaotic. However, unlike the previous case, there is no monotonic dependence between the varying parameter and the maximum Lyapunov exponent. This can be explained by the high complexity of the system, in which the thickness of the panels affects a

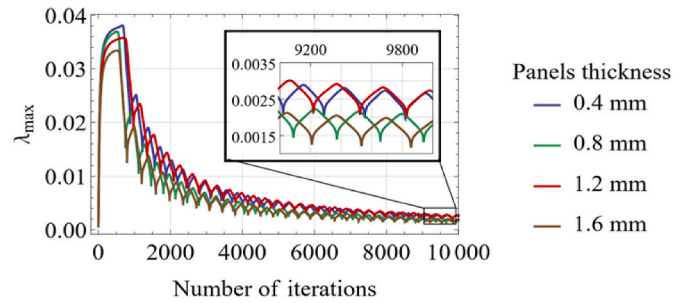


**Fig. 14.** Maximum Lyapunov exponents for the example CubeSat with panels of four different thicknesses.

large number of system parameters, e.g., the frequency of the oscillations of the panels, moments of inertia, position of the CoM of the satellite. The latter, in its turn, strongly affects the aerodynamic coefficients. It has to be mentioned here that the problem of quantitative assessment of the propensity of the described system to chaotic behavior depending on various parameters is challenging, so the above numerical examples must be considered exemplary rather than exhaustive.

Thus, numerical simulations confirm the possibility of chaos in attitude motion of an aerodynamically stabilized satellite with tail panels, even in low orbits.

### 5. Conclusion

This paper reveals some features of the nonlinear attitude dynamics of CubeSats with deployable stabilizing panels in low orbits. It was shown that, in the presence of the intermediate unstable equilibrium positions, instead of stabilizing the attitude motion of the satellite, the oscillating panels may paradoxically destabilize it due to chaos. The satellite may get to one of the intermediate positions because of an accidental disturbance, e.g., during the separation from the launch vehicle. Therefore, obviously, it is preferable to eliminate these positions at the design phase. In the cases where this is not possible, the risk of large disturbances causing angular oscillations of the satellite with large amplitudes should be minimized. Another way is to use additional devices (reaction wheels, magnetorquers, etc.) to compensate the undesirable aerodynamic features. The results of the paper can be used to select the parameters of these devices. It is also demonstrated that, for studying the attitude oscillations at high angles of attack, it is important not to neglect the damping aerodynamic torque, since, if the satellite has intermediate trim positions, damping may lead to qualitatively different motions.

The future work will focus on certain related problems not covered in this paper. In particular, it is interesting to study a more general case of three-dimensional attitude motion of CubeSats with flexible side panels in free molecular flow. This case may contain new chaotic effects related to the decomposition of the satellite rotation about the center of mass into nutation, precession, and spin. Another important area of research is the determination of the boundaries of chaotic regions in the phase portrait for different combinations of system parameters. Furthermore, the dynamics of panels deployment needs to be investigated.

### Declaration of competing interest

The authors declare that they have no known competing financial interests or personal relationships that could have appeared to influence the work reported in this paper.

### Acknowledgements

This study was supported by the Russian Science Foundation (Project No. 19-19-00085).

## References

- [1] A. Poghosyan, A. Golkar, CubeSat evolution: analyzing CubeSat capabilities for conducting science missions, *Prog. Aero. Sci.* 88 (2017) 59–83, <https://doi.org/10.1016/j.paerosci.2016.11.002>.
- [2] T. Villela, C.A. Costa, A.M. Brandão, F.T. Bueno, R. Leonardi, Towards the thousandth CubeSat: a statistical overview, *Int. J. Aerosp. Eng.* 2019 (2019) 1–13, <https://doi.org/10.1155/2019/5063145>.
- [3] E. Kulu, Nanosatellite & CubeSat Database, 2020. <http://www.nanosats.eu/>. (Accessed 28 September 2020).
- [4] K. Woellert, P. Ehrenfreund, A.J. Ricco, H. Hertzfeld, Cubesats: cost-effective science and technology platforms for emerging and developing nations, *Adv. Space Res.* 47 (2011) 663–684, <https://doi.org/10.1016/j.asr.2010.10.009>.
- [5] P. Kaaret, A. Zajczyk, D.M. LaRocca, R. Ringuette, J. Bluem, W. Fuelberth, H. Gulick, K. Jahoda, T.E. Johnson, D.L. Kirchner, others, HaloSat: a Cubesat to study the hot galactic halo, *Astrophys. J.* 884 (2019) 162.
- [6] M.I. Desai, F. Allegrini, R.W. Ebert, K. Ogasawara, M.E. Epperly, D.E. George, E. R. Christian, S.G. Kanekal, N. Murphy, B. Randol, The CubeSat mission to study solar particles, *IEEE Aero. Electron. Syst. Mag.* 34 (2019) 16–28.
- [7] A. Capannolo, G. Zanotti, M. Lavagna, E.M. Epifani, E. Dotto, V. Della Corte, I. Gai, M. Zannoni, M. Amoroso, S. Pirrotta, Challenges in LICIA Cubesat trajectory design to support DART mission science, *Acta Astronaut.* (2020), <https://doi.org/10.1016/j.actaastro.2020.09.023>.
- [8] J. Pezent, R. Sood, A. Heaton, High-fidelity contingency trajectory design and analysis for NASA's near-earth asteroid (NEA) Scout solar sail Mission, *Acta Astronaut.* 159 (2019) 385–396, <https://doi.org/10.1016/j.actaastro.2019.03.050>.
- [9] N. Saeed, A. Elzanaty, H. Almorad, H. Dahrouj, T.Y. Al-Naffouri, M.-S. Alouini, Cubesat communications: recent advances and future challenges, *IEEE Commun. Surv. & Tutorials.* 22 (2020) 1839–1862.
- [10] E. Peral, S. Tanelli, Z. Haddad, O. Sy, G. Stephens, E. Im, Raincube: a proposed constellation of precipitation profiling radars in CubeSat, *IEEE Int. Geosci. Remote Sens. Symp.* 2015 (2015) 1261–1264.
- [11] J.L. Forshaw, G.S. Aglietti, T. Salmon, I. Retat, M. Roe, C. Burgess, T. Chabot, A. Pisseloup, A. Phipps, C. Bernal, F. Chaumette, A. Pollini, W.H. Steyn, Final payload test results for the RemoveDebris active debris removal mission, *Acta Astronaut.* 138 (2017) 326–342, <https://doi.org/10.1016/j.actaastro.2017.06.003>.
- [12] C. Underwood, A. Viquerat, M. Schenk, B. Taylor, C. Massimiani, R. Duke, B. Stewart, S. Fellowes, C. Bridges, G. Aglietti, B. Sanders, D. Masutti, A. Denis, InflateSail de-orbit flight demonstration results and follow-on drag-sail applications, *Acta Astronaut.* 162 (2019) 344–358, <https://doi.org/10.1016/j.actaastro.2019.05.054>.
- [13] D. Selva, D. Krejci, A survey and assessment of the capabilities of Cubesats for Earth observation, *Acta Astronaut.* 74 (2012) 50–68, <https://doi.org/10.1016/j.actaastro.2011.12.014>.
- [14] M. Pastena, M. Tossaint, A. Regan, M. Castorina, P. Philippe, J. Rosello, A. Gabriele, N. Melega, Overview of ESA's Earth Observation upcoming small satellites missions. 34th Annual AIAA/USU Conf, Small Satell., 2020, pp. 1–8. [https://digitalcommons.usu.edu/small\\_sat/2020/all2020/127/](https://digitalcommons.usu.edu/small_sat/2020/all2020/127/).
- [15] M. Leomanni, A. Garulli, A. Giannitrapani, F. Scortecci, Propulsion options for very low Earth orbit microsats, *Acta Astronaut.* 133 (2017) 444–454, <https://doi.org/10.1016/j.actaastro.2016.11.001>.
- [16] N.H. Crisp, P.C.E. Roberts, S. Livadiotti, V.T.A. Oiko, S. Edmondson, S.J. Haigh, C. Huyton, L.A. Sinpetru, K.L. Smith, S.D. Worrall, others, The benefits of very low earth orbit for earth observation missions, *Prog. Aero. Sci.* 117 (2020) 100619, <https://doi.org/10.1016/j.paerosci.2020.100619>.
- [17] J. Li, M. Post, T. Wright, R. Lee, Design of attitude control systems for CubeSat-class nanosatellite, *J. Control Sci. Eng.* 2013 (2013), <https://doi.org/10.1155/2013/657182>.
- [18] N.A. Gatsonis, Y. Lu, J. Blandino, M.A. Demetriou, N. Paschalidis, Micropulsed plasma thrusters for attitude control of a low-earth-orbiting CubeSat, *J. Spacecr. Rockets.* 53 (2016) 57–73.
- [19] D.B. DeBra, The effect of aerodynamic forces on satellite attitude, *J. Astronaut. Sci.* 6 (1959) 40–45.
- [20] J.K. Wall, The feasibility of aerodynamic attitude stabilization of a satellite vehicle, *Am. Rocket Soc. Prepr.* (1959).
- [21] V.V. Beletskii, Motion of an Artificial Satellite about its Center of Mass, vol. 429, NASA TT F, 1966.
- [22] L. Meirovitch, F.B. Wallace Jr., On the effect of aerodynamic and gravitational torques on the attitude stability of satellites, *AIAA J* 4 (1966) 2196–2202, <https://doi.org/10.2514/3.3876>.
- [23] V.A. Sarychev, Aerodynamic stabilization system of the satellite, *Proc. Int. Conf. Attitude Chang. Stab. Satell.* (1968) 177–183.
- [24] M.A. Frik, Attitude stability of satellites subjected to gravity gradient and aerodynamic torques, *AIAA J* 8 (1970) 1780–1785, <https://doi.org/10.2514/6.1969-832>.
- [25] R.R. Kumar, D.D. Mazanek, M.L. Heck, Parametric and classical resonance in passive satellite aerostabilization, *J. Spacecr. Rockets.* 33 (1996) 228–234.
- [26] QARMAN - QubeSat for aerothermodynamic research and measurements on Ablation (n.d.), <https://www.vki.ac.be/index.php/qarman-home>.
- [27] others N.H. Crisp, P.C.E. Roberts, S. Livadiotti, A.M. Rojas, V.T.A. Oiko, S. Edmondson, S.J. Haigh, B.E.A. Holmes, L.A. Sinpetru, K.L. Smith, In-orbit aerodynamic coefficient measurements using SOAR (Satellite for Orbital Aerodynamics Research), *Acta Astronaut.* 180 (2021) 85–99.
- [28] M.L. Psiaki, Nanosatellite attitude stabilization using passive aerodynamics and active magnetic torquing, *J. Guid. Control. Dyn.* 27 (2004) 347–355.
- [29] S.A. Rawashdeh, J.E. Lumpp, Aerodynamic stability for CubeSats at ISS orbit, *J. Small Satell.* 2 (2013) 85–104.
- [30] T. Scholz, P. Rambaud, C. Asma, Design of an aerodynamic stability and de-orbiting system for cubesats, *RAST 2013 - Proc. 6th Int. Conf. Recent Adv. Sp. Technol.* (2013) 893–897, <https://doi.org/10.1109/RAST.2013.6581340>.
- [31] R. Sutherland, I. Kolmanovsky, A.R. Girard, Attitude control of a 2U Cubesat by magnetic and air drag torques, *IEEE Trans. Control Syst. Technol.* 27 (2018) 1047–1059.
- [32] D. Guglielmo, S. Omar, R. Bevilacqua, L. Fineberg, J. Treptow, B. Poffenberger, Y. Johnson, Drag deorbit device: a new standard reentry actuator for CubeSats, *J. Spacecr. Rockets.* 56 (2019) 129–145, <https://doi.org/10.2514/1.A34218>.
- [33] S.R. Omar, R. Bevilacqua, Hardware and GNC solutions for controlled spacecraft re-entry using aerodynamic drag, *Acta Astronaut.* 159 (2019) 49–64, <https://doi.org/10.1016/j.actaastro.2019.03.051>.
- [34] S.S. Kedare, S. Ulrich, Undamped passive attitude stabilization and orbit management of a 3U cubesat with drag sails, *Adv. Astronaut. Sci.* 156 (2016) 1231–1248.
- [35] M. Berthet, K. Yamada, Y. Nagata, K. Suzuki, Feasibility assessment of passive stabilisation for a nanosatellite with aeroshell deployed by orbit-attitude-aerodynamics simulation platform, *Acta Astronaut.* 173 (2020) 266–278.
- [36] J. Walsh, L. Berthoud, C. Allen, Drag reduction through shape optimisation for satellites in very low earth orbit, *Acta Astronaut.* 179 (2021) 105–121, <https://doi.org/10.1016/j.actaastro.2020.09.018>.
- [37] V. Aslanov, D. Sizov, 3U CubeSat aerodynamic design aimed to increase attitude stability and orbital lifetime, in: 71st Int. Astronaut. Congr., 2020.
- [38] P.B. Grote, J.E. McMunn, R. Gluck, Equations of motion of flexible spacecraft, *J. Spacecr. Rockets.* 8 (1971) 561–567, <https://doi.org/10.2514/3.59693>.
- [39] J.L. Junkins, Y. Kim, Introduction to Dynamics and Control of Flexible Structures, American Institute of Aeronautics and Astronautics, 1993.
- [40] A.J. Miller, G.L. Gray, A.P. Mazzoleni, Nonlinear spacecraft dynamics with a flexible appendage, damping, and moving internal submasses, *J. Guid. Control. Dyn.* 24 (2001) 605–615, <https://doi.org/10.2514/2.4752>.
- [41] V.S. Aslanov, V.V. Yudin, Behavior of tethered debris with flexible appendages, *Acta Astronaut.* 104 (2014) 91–98.
- [42] V.S. Aslanov, V.V. Yudin, Dynamics, analytical solutions and choice of parameters for towed space debris with flexible appendages, *Adv. Sp. Res.* 55 (2015) 660–667.
- [43] R. Qi, Y. Zhang, S. Lu, Q. Hu, R. Zhong, Tethered towing of defunct satellites with solar panels, *Acta Astronaut.* 175 (2020) 1–10.
- [44] P.J. Holmes, J.E. Marsden, Horseshoes and Arnold diffusion for Hamiltonian systems on Lie groups, *Indiana Univ. Math. J.* 32 (1983) 273–309.
- [45] B.-Z. Yue, Study on the chaotic dynamics in attitude maneuver of liquid-filled flexible spacecraft, *AIAA J* 49 (2011) 2090–2099.
- [46] M. Chegini, H. Sadati, Chaos analysis in attitude dynamics of a satellite with two flexible panels, *Int. J. Non. Linear. Mech.* 103 (2018) 55–67.
- [47] V.S. Aslanov, Dynamics of a satellite with flexible appendages in the Coulomb interaction, *J. Guid. Control. Dyn.* 41 (2018) 565–572.
- [48] V.S. Aslanov, Chaotic attitude dynamics of a LEO satellite with flexible panels, *Acta Astronaut.* 180 (2021) 538–544.
- [49] S. Omar, C. Riano-Rios, R. Bevilacqua, The drag maneuvering device for the semi-passive three-axis attitude stabilization of low earth orbit nanosatellites, *J. Small Satell.* to appear. (2021).
- [50] B. Chen, H. Zhan, W. Zhou, Aerodynamic design of a re-entry capsule for high-speed manned re-entry, *Acta Astronaut.* 106 (2015) 160–169.
- [51] G. Zuppardi, R. Savino, G. Mongelluzzo, Aero-thermo-dynamic analysis of a low ballistic coefficient deployable capsule in Earth re-entry, *Acta Astronaut.* 127 (2016) 593–602.
- [52] A.D. Santangelo, G.E. Johnson, Optimal wing configuration of a Tethered Satellite system in free molecular flow, *J. Spacecr. Rockets.* 29 (1992) 668–670.
- [53] D. Mostaza-Prieto, P.C.E. Roberts, Methodology to analyze attitude stability of satellites subjected to aerodynamic torques, *J. Guid. Control. Dyn.* 39 (2016) 437–449.
- [54] R.G. Wilmoth, R.A. Mitcheltree, J.N. Moss, Low-density aerodynamics of the stardust sample return capsule, *J. Spacecr. Rockets.* 36 (1999) 436–441, <https://doi.org/10.2514/2.3464>.
- [55] S.A. Schaaf, P.L. Chambre, Flow of rarefied gases, high speed aerodynamics and jet propulsion, in: *Fundam. Gas Dyn.*, Princeton University Press, NY, 1958.
- [56] F.J. Regan, S.M. Anandakrishnan, Dynamics of Atmospheric Re-entry, American Institute of Aeronautics and Astronautics, 1993.
- [57] S.F. Rafano Carná, R. Bevilacqua, High fidelity model for the atmospheric re-entry of CubeSats equipped with the Drag De-Orbit Device, *Acta Astronaut.* 156 (2019) 134–156, <https://doi.org/10.1016/j.actaastro.2018.05.049>.
- [58] P. Gallais, Atmospheric Re-entry Vehicle Mechanics, Springer Science & Business Media, 2007.
- [59] S.G. Kelly, Fundamentals of Mechanical Vibrations, McGraw Hill, 2000.
- [60] V.K. Melnikov, On the stability of the center for time periodic perturbations, *Trans. Moscow Math. Soc.* 12 (1963) 3–52.
- [61] S. Wiggins, Introduction to Applied Nonlinear Dynamical Systems and Chaos, Springer Science & Business Media, 2003.
- [62] International standard ISO 14222:2013, Space Environment (Natural and Artificial) — Earth Upper Atmosphere, 2013. <https://www.iso.org/standard/54507.html>.

- [63] P.M. Mehta, A. Walker, C.A. McLaughlin, J. Koller, Comparing physical drag coefficients computed using different gas–surface interaction models, *J. Spacecr. Rockets*. 51 (2014) 873–883.
- [64] J.P. Mason, B. Lamprecht, T.N. Woods, C. Downs, CubeSat on-orbit temperature comparison to thermal-balance-tuned-model predictions, *J. Thermophys. Heat Transf.* 32 (2018) 237–255.
- [65] C. Skokos, The Lyapunov characteristic exponents and their computation, in: *Dyn. Small Sol. Syst. Bodies Expl.*, Springer, 2010, pp. 63–135.